Object-Based Superresolution Land-Cover Mapping From Remotely Sensed Imagery

Chen, Y., Ge, Y., Heuvelink, G. B. M., An, R., & Chen, Y.

Chen, Y., Ge, Y., Heuvelink, G. B. M., An, R., & Chen, Y. (2018). Object-Based Superresolution Land-Cover Mapping From Remotely Sensed Imagery. IEEE Transactions on Geoscience and Remote Sensing, 56(1), 328-340. DOI: 10.1109/TGRS.2017.2747624

Object-Based Super-Resolution Land Cover Mapping From Remotely Sensed Imagery

Journal:	*Transactions on Geoscience and Remote Sensing*
Manuscript ID	TGRS-2016-01081
Manuscript Type:	Regular paper
Date Submitted by the Author:	16-Oct-2016
Complete List of Authors:	Chen, Yuehong; Institute of Geographical Sciences & Natural Resources Research, State Laboratory of Resources & Environmental Information System,Chinese Academy of Sciences Ge, Yong; Institute of Geographical Sciences & Natural Resources Research, State Laboratory of Resources & Environmental Information System,Chinese Academy of Sciences Heuvelink, Gerard; Wageningen University, Land Dynamics Group An, Ru; HoHai University, Geographic information system Chen, Yu; Nanjing Normal University, School of Geography Science
Keywords:	Remote sensing

Object-Based Super-Resolution Land Cover Mapping From Remotely Sensed Imagery

Yuehong Chen, Yong Ge*, *Member*, *IEEE*, Gerard B.M. Heuvelink, Ru An, and Yu Chen

***Abstract*—Super resolution mapping (SRM) is a widely used technique to address mixed pixel problem in pixel-based classification. Advanced object-based classification will face the similar mixed phenomenon—mixed object that contains different land-cover classes. Currently, most SRM approaches focus on handling mixed pixels in pixel-based classification. Little if any consideration has been given to predict where classes spatially distribute within mixed objects. This article, therefore, proposes a new object-based super resolution mapping strategy (OSRM) to deal with mixed objects in object-based classification. First, it uses the deconvolution technique to estimate the semivariograms at target subpixel scale from the class proportions of irregular objects. Then, area-to-point kriging method is applied to predict the soft class values of subpixels within each irregular object according to the estimated semivariograms and the class proportions of objects. Finally, a linear optimization model at object-level is built to determine the optimal class labels of subpixels. Two synthetic images and a real remote sensing image were used to evaluate the performance of OSRM. The experimental results demonstrated that OSRM performed better and generated more land-cover details within mixed objects than the traditional object-based hard classification. Hence, OSRM provides a valuable solution to mixed objects in object-based classification.**

***Index Terms*—Super resolution mapping, mixed object, remotely sensed imagery, deconvolution, area-to-point kriging**

I. Introduction

Extraction of land-use/land-cover maps from remote sensing imagery is critical for environmental monitoring requirements and natural resources management [1]. Image classification is a widely used technique for this purpose [2]. After the launch of Landsat-1 satellite in 1972, a series of remote sensing image classification approaches were soon developed especially during

This work was supported by the National Natural Science Foundation of China under Grant 41471296 (Corresponding author: Yong Ge).

Y. Chen is with the School of Earth Sciences and Engineering, Hohai University, Nanjijng 210098, China and also with the State Key Laboratory of Resources and Environmental Information System, Institute of Geographical Sciences and Natural Resources Research, University of Chinese Academy of Sciences, Beijing 100101, China (e-mail: chenyh@lreis.ac.cn).

Y. Ge is with the State Key Laboratory of Resources and Environmental Information System, Institute of Geographical Sciences and Natural Resources Research, University of Chinese Academy of Sciences, Beijing 100101, China and also with Jiangsu Center for Collaborative Innovation in Geographical Information Resource Development and Application, Nanjing 210023, China(e-mail: gey@lreis.ac.cn).

G. B. M. Heuvelink is with the Soil Geography and Landscape group, Wageningen University, The Netherlands (e-mail: gerard.heuvelink@wur.nl).

R. An is with School of Earth Science and Engineering, Hohai University, Nanjijng 210098, China (anrunj@163.com).

Yu Chen is with School of Geography Science, Nanjing Normal University, Nanjing 210023, China (chenyu@lreis.ac.cn).

1980s and 1990s [2], including unsupervised classifiers (e.g., k-means and ISODATA) and supervised classifiers (e.g., maximum likelihood and decision tree). In this stage, remote sensing image classifiers mainly depend on spectral features and assign single pixels to single classes. They are often termed as per-pixel classifiers (or hard classifiers) because they assume each pixel is pure and classify pixels into mutually exclusive land-cover classes pixel-by-pixel [2]. However, such an assumption is usually invalid for medium and low spatial resolution remote sensing imagery because of the presence of a large number of mixed pixels that contain more than one land-cover class [3]. Meanwhile per-pixel classifiers may result in a loss of information and limited accuracies when handling mixed pixels [4]. Since the early 1990s, per-subpixel classification (also termed as soft classification or spectral unmixing) approaches have become prevailing to address mixed pixel problem as they can provide the proportions (i.e., possibilities of class occurrence for each pixel) for different classes within a pixel [2]. Even so, per-subpixel classification approaches still estimate the class proportions with the pixel as the basic analysis unit. Thus, both per-pixel and per-subpixel classifiers can be considered as pixel-based classifiers [5]. With the development of remote sensing technology, a series of high and very-high spatial resolution remote sensing satellites, such as SPOT5 and IKONOS, launched close on another. Pixel-based classification techniques, when they are used to deal with these high and very-high spatial resolution images, are criticized due to the severe salt and pepper effect in classified maps [5]. As a result, object-based classification techniques, a new processing paradigm of these high resolution images, were developed since the early 21st century [5]. Object-based classifiers group several pixels with similar features into an object and consider the object, instead of individual pixels, as the basic analysis unit.

A major problem that using pixel-based classifiers to classify low and medium spatial resolution remote sensing imagery is mixed pixels [2, 3]. Fortunately, super resolution mapping (SRM) (also termed as subpixel mapping) technique is proposed as a promising solution to mixed pixels [4]. SRM fist disaggregates each coarse pixel in fractional images (i.e., the output of pixel-based soft classification) into fine subpixels and then determines where the subpixels of each land-cover class spatially distribute within a pixel [6-12]. Over the past decades, many SRM methods have been proposed. These methods involve the pixel swapping algorithm [7, 13], Hopfield neural networks [14-16], subpixel/pixel spatial attraction models [17-19], Markov random fields [20-23], the geometric methods [24, 25], geostatistical methods [26-28], artificial intelligence-based algorithms [29-33] and interpolation-based methods [34-36]. These methods have obtained acceptable performances in various applications, such as urban tree identification [37], urban building extraction [38], floodplain inundation mapping [39, 40] and land use mapping [41]. Mixed pixels cannot avoid as well when classifying high and very-high remote sensing imagery by object-based classifiers. Because whatever the spatial resolution of remote sensing imagery is, the intersection areas of different land-cover classes often result in mixed pixels [3, 5, 42], as shown in Fig. 1. Fig. 1(a) shows a simulated land-cover area with four land-cover classes—buildings, forest, bush and water. Fig. 1(b)-(d) present the simulated images with different spatial resolutions for Fig. 1(a). It can be observed from Fig. 1 that mixed pixels usually exist in the intersection areas of any spatial resolution imagery even the spatial resolution

continues to increase.

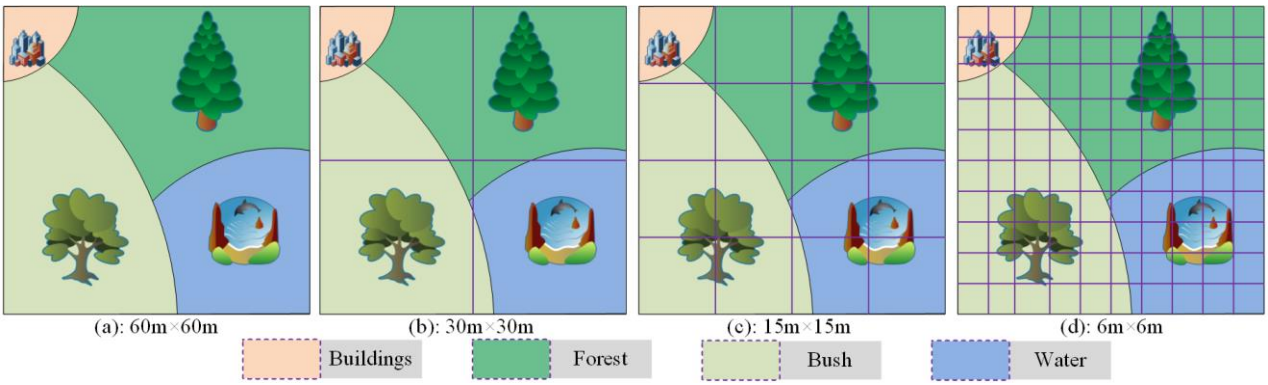

Fig. 1. Mixed pixels in different spatial resolution remote sensing imagery. (a) A simulated land-cover image with the size of 60m×60m; (b) 30m spatial resolution image for (a); (c) 15m spatial resolution image for (a); (d) 6m spatial resolution image for (a).

Addressing mixed pixel problem is important for pixel-based classification [2, 3], while object-based classification would need to solve "mixed object" problem—the analogue of mixed pixel problem—as it considers the object as the basic analysis unit. Mixed object problem may be caused by two major reasons. The first reason is aforementioned mixed pixel problem. These mixed pixels at the intersection area of classes belong to the high-resolution (H-resolution) type [42], where pixels are smaller than the objects of interest (see Fig. 1(d)). They have a large proportion in high and very high resolution images because higher resolution images may lead to more objects that are larger than the pixel size and because many low-resolution (L-resolution) mixed pixels in coarse images [42], whose size is larger than the objects of interest, can be transformed into H-resolution cases in fine images (see Fig. 1(b)-(d)). Fig. 2(a) shows a mixed object marked by the red polygon, which is caused by mixed pixels in the intersection area between water and vegetation. Image segmentation is another important reason. In object-based classification, image segmentation is a critical process to create the basic analysis units of objects from remote sensing images. Although there has been developed numerous methods for this purpose, under-segmentation is still a common phenomenon in segmentation results due to many factors, such as weights of object shape and spectra [43], and the segmentation scale parameter [44]. For example, Fig. 2(b) shows a mixed object of water and vegetation classes marked by the red polygon and it is also an under-segmentation mixed object. SRM has been demonstrated as an effective way to handle the mixed pixels in pixel-based classification [4, 10-12, 19, 24], while there is no a solution to mixed objects in object-based classification process. It is, therefore, necessary to develop a technique to handle the mixed object problem for classifying high and very high spatial resolution remote sensing imagery by object-based classification.

The objective of this paper is to propose an object-based super resolution mapping (OSRM) approach to solve the mixed object problem in object-based classification. Based on the output (i.e., class proportions for each object) of objet-based soft classification, OSRM first divides each pixel within a mixed object into subpixels according to the target zoom scale factor, and then it predicts where the subpixels of each land-cover class spatially locate within the mixed object. OSRM employs area-to-point kriging (ATPK) to predict the soft class values (i.e., possibilities of class occurrence) of subpixels within an object because ATPK is able to handle

the irregular areal data of objects with different shapes and sizes [45, 46]. Meanwhile, under the assumption of spatial dependence, ATPK uses the spatial relationships of neighboring objects in predicting the soft class values of subpixels within the object under consideration. Deconvolution technique on irregular areal data is applied to generate the point support (i.e., the target zoom scale) semivariogram of each class from the class proportions of objects as ATPK needs the point support semivariogram as input [47]. After ATPK, a linear optimization model is built to determine the optimal land-cover labels of subpixels within an object by maximizing the sum of soft class values of subpixels, constrained from the class proportions of object-based soft classification. Compared with traditional SRM methods, OSRM has several characteristics and differences: 1) it inherits the idea of traditional SRM methods through predicting the spatial distribution of land-cover classes at the subpixel scale and reducing the location uncertainty of subpixels to solve the mixed object problem; 2) it is the post-processing of object-based soft classification whereas traditional SRM is the post-processing of pixel-based soft classification; 3) it performs with the irregular areal data of objects, rather than regular pixels in traditional SRM methods, as the basic analysis units; 4) it employs ATPK and deconvolution to consider the spatial relationships of neighboring irregular objects because ATPK and deconvolution are two state-of-the-art geostatistical tools for handling the irregular areal datasets.

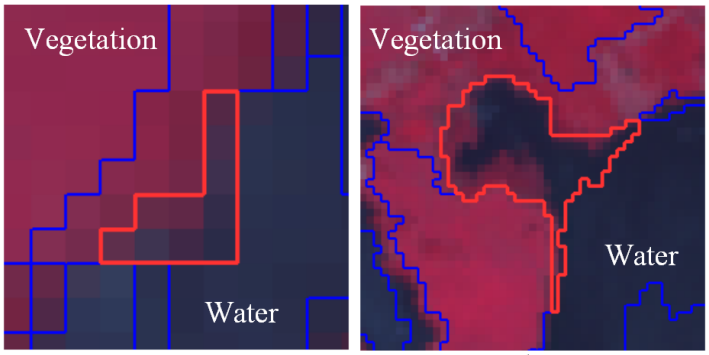

Fig. 2. Mixed objects. (a) A mixed object (the red polygon) caused by mixed pixels. (b) A mixed object (the red polygon) caused by image segmentation.

The remainder of this paper is organized as follows. Section II describes the proposed method. Section III shows experimental results and discussed in Section IV. Section V presents conclusions.

II. Methodology

Let $Y=\{y_i \mid i=1,...,m\}$ be the original coarse remote sensing image with m pixels. Image segmentation partitions Y into R un-overlapping objects $O=\{O_r \mid r=1,...,R\}$, where O_r is a non-empty polygon consisting of a group of pixels $\{y_i \mid i=1,...,n_r\}$. Implementing object-based soft classification on objects O, the class proportions $\{O_r^c \mid c=1,...,C\}$ of object O_r is obtained, where C is the number of land-cover classes. By setting the zoom scale factor S and using the class proportions of objects O as inputs, OSRM yields a fine spatial resolution land-cover map $X=\{x_j^c \mid j=1,...,M$ and $M=m\times S^2\}$, through dividing each coarse pixel

into $S \times S$ fine subpixels. Now, $x_j^c \in \{0,1\}$ is defined by Eq. (1) below, which indicates that subpixel j is a logical value that means whether it belongs to land-cover class c.

$$x_j^c = \begin{cases} 1, & \text{subpixel } j \text{ is classified to class } c \\ 0, & \text{otherwise} \end{cases} \tag{1}$$

With the output of object-based soft classification as input, OSRM performs through three main parts: 1) generating the point support semivariogram of each land-cover class from the class proportions of objects by deconvolution; 2) implementing ATPK to obtain the soft class values of subpixels within each object; 3) determining the optimal land-cover labels of subpixels by a linear optimization model. In this paper, the areal support data is the output (i.e., object's class proportions) of object-based soft classification whereas the point support data is the OSRM map at the subpixel scale. That is to say areas correspond to objects whereas points corresponds to subpixels.

A. Generating the Point Support Semivariograms by Deconvolution

Deconvolution is an effective way to obtain point support semivariograms for ATPK because prior training data for deriving the point support semivariogram is often unavailable [8, 28]. Deconvolution aims to iteratively seek a point support semivariogram that minimizes the difference between the theoretically regularized semivariogram and the areal support semivariogram fitted to areal data [47]. Deconvolution is suitable for both regular and irregular data. Wang, et al. [28] performed it on the regular data of remote sensing images and achieved satisfactory results. Goovaerts [47] provided a practical implementation of deconvolution on irregular areal data. As the object-based soft classification results are irregular polygons with different shape and size, thus the deconvolution technique on irregular areal data is used here in deriving the point support semivariogram for ATPK.

Let $\gamma_O^c(h)$ be the areal support (i.e., the object scale) semivariogram for class c fitted to the class proportion of objects and $\gamma_x^c(h)$ be the point support (i.e., the subpixel scale) semivariogram for class c, where h is the lag distance. Following the well-known regularization theory [48], the point support semivariogram $\gamma_x^c(h)$ can be convolved to the regularized semivariogram $\gamma_{OR}^c(h)$ at the areal support as

$$\gamma_{OR}^c(h) = \bar{\gamma}_{OO}^c(O^c, O_h^c) - \bar{\gamma}_{OO}^c(O^c, O^c) \tag{2}$$

The first term in Eq.(2), area-to-area semivariogram $\bar{\gamma}_{OO}^c(O^r, O_h^c)$, represents the mean value of the point support semivariogram between an arbitrary point in object O^c and another point in object O_h^c. It is estimates as

$$\bar{\gamma}_{OO}^{c}(O^{c},O_{h}^{c})=\frac{1}{N_{h}}\sum_{r=1}^{N_{h}}\bar{\gamma}_{O}^{c}(O_{r}^{c},O_{r+h}^{c})$$
$$\bar{\gamma}_{O}^{c}(O_{r}^{c},O_{r+h}^{c})=\frac{1}{N_{r}N_{r+h}}\sum_{j=1}^{N_{r}}\sum_{j'=1}^{N_{r+h}}\gamma_{x}^{c}(x_{j}^{c},x_{j'}^{c}) \quad (3)$$

where, N_h is the number of paired objects at the lag of h. N_r, N_{r+h} are the numbers of points within the two objects O_r^c, O_{r+h}^c, respectively. $\gamma_x^c(x_j^c, x_{j'}^c)$ is the semivariogram value at the point support.

The second term in Eq.(2), within-area semivariogram $\bar{\gamma}_{OO}^{c}(O^{c},O^{c})$, represents the semivariogram mean value of the point pairs within the areal support of object O^c. When all the areas have the same size and shape, it is a constant [28]. If areas have different size and shape, on the other hand, it varies as a function of distance h [47] as

$$\bar{\gamma}_{OO}^{c}(O^{c},O^{c})=\frac{1}{2N_{h}}\sum_{r=1}^{N_{h}}\left(\bar{\gamma}_{O}^{c}(O_{r}^{c},O_{r}^{c})+\bar{\gamma}_{O}^{c}(O_{r+h}^{c},O_{r+h}^{c})\right) \quad (4)$$

where $\bar{\gamma}_{O}^{c}(O_{r}^{c},O_{r}^{c}), \bar{\gamma}_{O}^{c}(O_{r+h}^{c},O_{r+h}^{c})$ are the mean values of the point support semivariogram between point pairs within the two objects, respectively. They can be estimated by Eq.(3).

Given an initial point semivariogram $\gamma_{x\_I}^{c}(h)$ for class c, deconvolution iteratively updates the point semivariogram to approximate its regularized semivariogram $\gamma_{OR}^{c}(h)$ with the fitted areal support semivariogram $\gamma_{O}^{c}(h)$ of objects. When the difference between $\gamma_{OR}^{c}(h)$ and $\gamma_{O}^{c}(h)$ meets the predefined terminal conditions, the optimal point semivariogram $\gamma_{x}^{c}(h)$ is achieved and can be used in the next process of ATPK for generating the soft class values of subpixels within an object. More details about the implementation of deconvolution on irregular areal data can be found in [47].

B. Obtaining the Soft Class Values of Subpixels by ATPK

Typical kriging approaches often use the centroid of geographical units for spatial proximity measurements in the interpolation, which is under the assumption that the spatial support of units has same size and shape [47, 48]. However the assumption is not suitable for irregular data with different shape and size. Recently, ATPK has been developed to solve this problem by incorporating the variable size and shape of areas in kriging [45]. ATPK accounts for the irregular spatial support through discretizing each area into several points, which are used to replace the centroid of each area in typical kriging methods [46]. ATPK estimates the soft class value p_j^c of subpixel j by the following linear combination of objects

$$p_j^c = \sum_{r=1}^{N} \lambda_r O_r^c \tag{5}$$

where N is the number of objects for the predication at subpixel j, λ_r is the weight assigned to object O_r^c. The weights are obtained by solving the following kriging system

$$\begin{cases} \sum_{r=1}^{N} \lambda_r \bar{C}(O_r^c, O_{r'}^c) + \mu_j = \bar{C}(p_j^c, O_r^c) \\ \sum_{r=1}^{N} \lambda_r = 1 \end{cases} \tag{6}$$

where $\bar{C}(p_j^c, O_r^c)$ is the area-to-point covariance, which is approximately calculated by the average of the point support covariance between the subpixel j and subpixels discretized in object O_r^c. A similar way is applied to calculate $\bar{C}(O_r^c, O_{r'}^c)$ as the average of the point support covariance between any two subpixels discretized in objects O_r^c and $O_{r'}^c$. μ_j is the Lagrange multiplier. Different from typical kriging approaches, ATPK needs the coherence constraint to ensure that the average of point estimates equals to the areal datum by

$$O_r^c = \frac{1}{N_r} \sum_{j=1}^{N_r} p_j^c \tag{7}$$

where N_r is the number of subpixels within object O_r^c.

C. Determining the Optimal Land-cover Labels of Subpixels

Traditional SRM methods often employ a binary integer programming model to determine the optimal land-cover labels of subpixels within each mixed pixel [19]. A similar model is built on each object in OSRM to obtain the optimal land-cover labels of subpixels. Based on maximizing the assumption of spatial dependence, the objective function in the model is defined in Eq.(8) to maximize the soft class values of the subpixels within each object, subjected to the class proportional constraints of each object in Eq. (9). Note that only mixed objects perform this model whereas the pure object is directly assigned to the same land-cover class to its all subpixels for saving computation time.

$$\text{maximize} \quad z = \sum_{j=1}^{N_r} \sum_{c=1}^{C} x_j^c \times p_j^c \tag{8}$$

$$\text{subject to} \begin{cases} \sum_{c=1}^{C} x_j^c = 1 \\ \sum_{j=1}^{N_r} x_j^c = N_r^c \\ N_r = m_r \times S^2 \\ N_r^c = O_r^c \times m_r \times S^2 \end{cases} \tag{9}$$

where N_r is the total number of subpixels within object O_r, p_j^c is the soft class value of subpixel j for class c by ATPK, m_r is the number of pixels within object O_r.

III. Experiments

A. Experimental Design

Three experiments on different images (two synthetic images and a real remote sensing image) were designed to evaluate the performance of OSRM. The two synthetic images are a 15-m ASTER image and a 6-m ZY-3 image, while the real image is an 8-m GF-1 image. Three object-based hard classification maps from each remote sensing image were obtained and used as reference maps for accuracy assessment. In the first two experiments on synthetic images, the original remote sensing images were first degraded into coarse images by each of the three testing scale factors (2, 3, and 4). Then, each degraded remote sensing image was used to obtain the objects by image segmentation with the segmentation scale parameter of 5 in eCognition software. Next, the object-based soft classification results (i.e., the class proportions of each object) were aggregated from reference maps through dividing the pixel number of each class within an object by the total pixel number of the object. Finally, OSRM was performed to obtain the SRM maps according to object-based soft classification results. Note that, in the two experiments, the object-based soft classification results were synthetic and error free. The aim of using synthetic class proportions of objects was to avoid the errors from object-based soft classification that would affect the evaluation of OSRM because many existing SRM methods used synthetic soft classification results in the evaluation [10, 12, 17, 28]. In the last experiment with the real GF-1 image, the class proportions of objects were directly derived from the real degraded GF-1 image by object-based soft classification and the scale factors of 2 and 4 were tested.

The object-based hard classification (OHC) results for each scale factor were used to visually compare with OSRM maps in the three experiments. The overall accuracy (OA) metric was employed to quantitatively assess the accuracy of classified maps. Note that the calculation of OA in the first two experiment was only for mixed objects to avoid the influence of pure objects as pure objects provided no useful information in evaluating SRM method [9, 29, 49]. Both object-based hard and soft classifiers are used the k-nearest neighbor approach when classifying spectral remote sensing images in the three experiments [50].

B. Experiment 1—Synthetic ASTER Imagery

Fig. 3(a) shows the multispectral ASTER image, having a spatial resolution of 15-m (360×360 pixels). Four main land-cover classes—water, grass, farmland and bareground, cover this area. Fig. 3(b) is the 15-m reference map generated by OHC from Fig. 3(a). The synthetic class proportions of each object were obtained as the input of OSRM from the reference map and image segmentation results for each scale factor. Fig. 4 shows examples of the synthetic object-based soft classified results using a scale factor of 2. With the class proportions of objects, deconvolution estimated the semivariograms of each class at target subpixel scale for ATPK. Fig. 5 presents the deconvolution results for the scale factor of 2. It can be seen that the regularized semivariogram (in green) is highly coincide with the semivariogram (in red) from the areal datasets of object-based soft classified results in Fig. 4 for each class, which indicates that deconvolution provided the reliable semivariograms (in blue) at target subpixel scale.

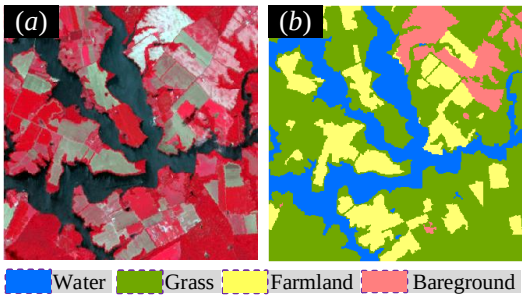

Fig. 3. Experiment on synthetic ASTER imagery. (a) ASTER imagery. (b) Reference land-cover map from (a).

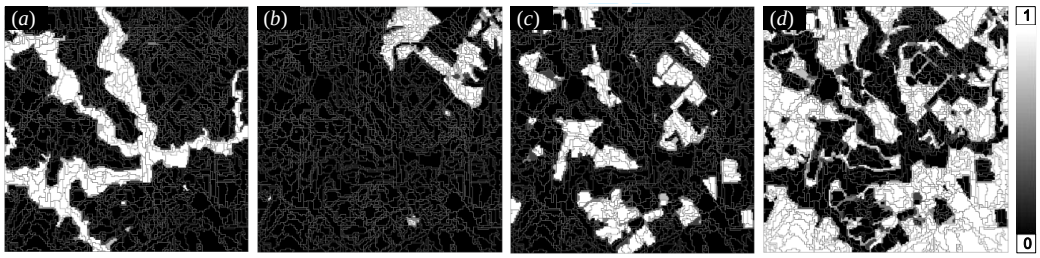

Fig. 4. Object-based soft classification results for synthetic ASTER imagery (*S*=2). (a) Water. (b) Bareground. (c) Farmland. (d) Grass.

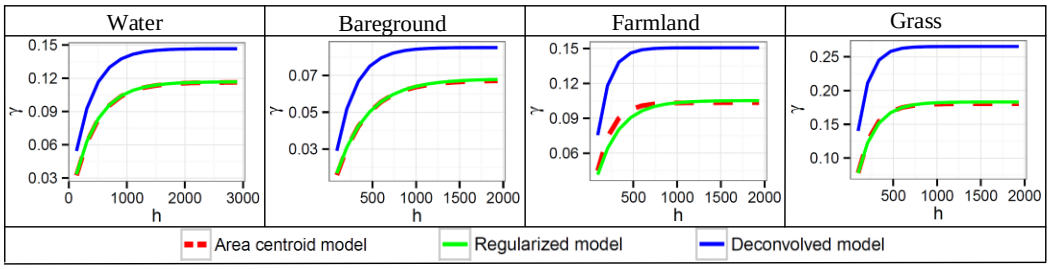

Fig. 5. Deconvolution results for synthetic ASTER imagery (*S*=2). The red dash, green solid and blue solid curves are the semivariograms from Fig. 4, regularized semivariograms, and the target point support (subpixel scale) semivariograms from deconvolution, respectively.

1) OSRM Results

Fig. 6 presents the examples of classified maps from the 30-m degraded ASTER image with the scale factor of 2 for illustration and analysis. Fig. 6(a) shows the synthetic OHC map at 30-m spatial resolution, while Fig. 6(b) presents the OSRM map with a

spatial resolution of 15-m. The synthetic OHC maps were generated by two steps: 1) convert the synthetic object-based soft classification results (e.g., Fig. 4) into object-based hard classified results; 2) transform the object-based hard classified results into raster hard classified map with the same spatial resolution of the degraded remote sensing image for each scale factor. It can be observed from Fig. 6 that the OSRM map in (b) has a significant improvement over the OHC result in (a). The OSRM map provides more details of land-cover patches and smoother boundaries of land-cover patches. Moreover, the OSRM map is more close to the reference map in Fig. 3(b) than the hard classified result. This can be well illustrated by classified results in the subarea of Fig. 6(i)-(iii). On visual inspection of Fig. 6(i)-(iii), it can be found that several small land-cover patches (e.g., the small water patch and the linear grass patch) are lost in (ii) whereas the OSRM map in (iii) well preserves them. Furthermore, the boundary of the water patch in Fig. 6(iii) is smoother than that in Fig. 6(ii). Therefore, based on visual assessment, OSRM produced more satisfactory classified maps than OHC because its results are more consistent with the reference map.

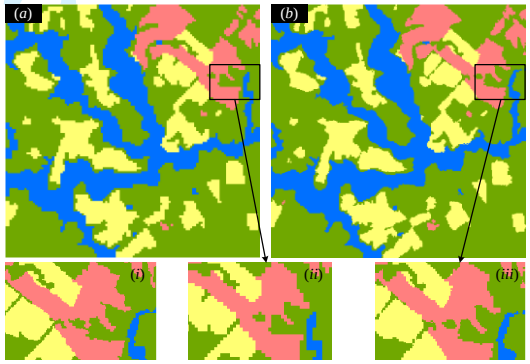

Fig. 6. Classification results for synthetic ASTER imagery (S=2). (a) OHC result. (b) OSRM map. (i) The reference map in the subarea marked by the black rectangle in (a) and (b). (ii)-(iii) Classified results in the subarea of (a) and (b), respectively.

2) Accuracy Assessment

Table I shows the accuracy assessment of classified maps for the synthetic ASTER imagery, and it confirms the findings from the visual assessment. Checking the accuracy in Table I, the OA of OSRM are over 81% whereas the OA of OHC are under 79% for all scale factors. OSRM produced significantly greater accuracy than OHC by an average OA gain of 4.24%. OSRM generated the greatest improvement of OA for S=2 by 6.12%. The OA gains of OSRM are 4.04% and 2.56% for the scale factor of 3 and 4, respectively. These improvements by OSRM were largely due to the fact that OSRM can predict the class spatial distribution within mixed objects and provide more land-cover details within mixed objects than the traditional object-based hard classification.

TABLE I
ACCURACY (OA) FOR THE SYNTHETIC ASTER IMAGERY (%)

	OHC	OSRM
S=2	78.35	84.47
S=3	78.91	82.95
S=4	78.81	81.37

C. *Experiment 2—Synthetic ZY-3 Imagery*

A 6-m multispectral ZY-3 image (360×360 pixels) was studied. The ZY-3 image in Fig. 7(a) mainly includes four land-cover classes of water, building, vegetation and bareground. The 6-m reference map in Fig. 7(b) was extracted from Fig. 7(a) by OHC and used in accuracy assessment. Fig. 8 displays the synthetic object-based soft classification results for the scale factor of 2. According to the synthetic object-based soft classification results, deconvolution was applied to estimate the target subpixel scale semivariograms of ATPK for each class. Fig. 9 exhibits the examples of deconvolution results for the scale factor of 2 and it indicates that deconvolution provided effective semivariograms at target subpixel scale as the good agreement between the regularized semivariogram from the target semivariograms and the areal semivariogram from Fig. 8 for each class.

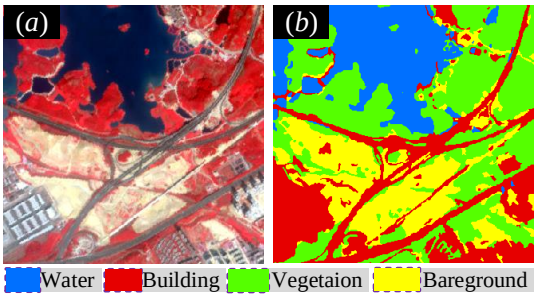

Fig. 7. Experiment on synthetic ZY-3 imagery. (a) ZY-3 imagery. (b) Reference land-cover map from (a).

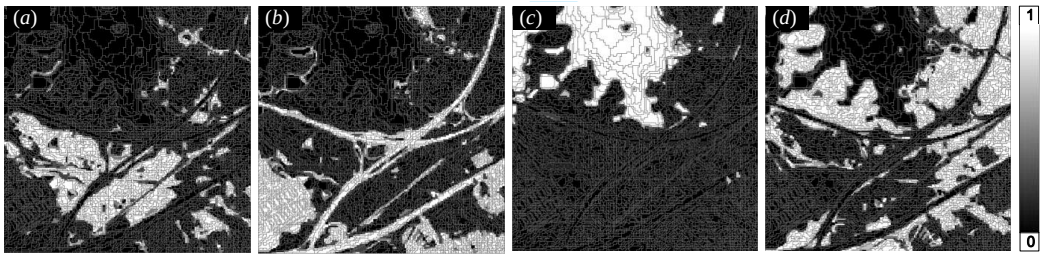

Fig. 8. Object-based soft classification results for synthetic ZY-3 imagery (*S*=2). (a) Bareground. (b) Building. (c) Water. (d) Vegetation.

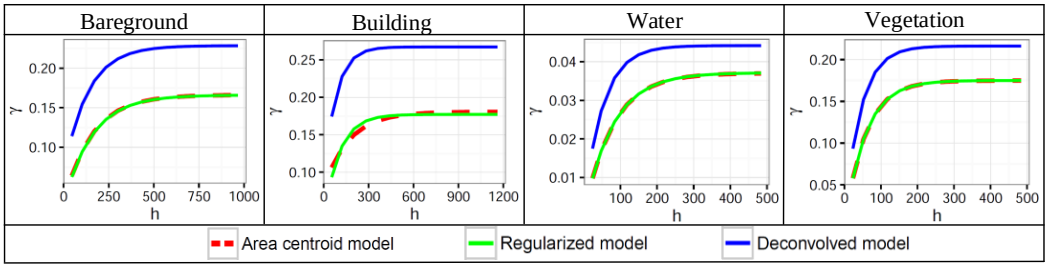

Fig. 9. Deconvolution results for synthetic ZY-3 imagery (*S*=2). The red dash, green solid and blue solid curves are the semivariograms from Fig. 8, regularized semivariograms, and the target point support (subpixel scale) semivariograms from deconvolution, respectively.

1) *OSRM Results*

The OHC result from Fig. 8 displays in Fig. 10(a). Fig. 10(b) presents the OSRM map for the scale factor of 2. When visually examining Fig. 10, it can be found that the OHC result once again had un-smoother boundaries of land-cover patches and lost many small land-cover patches whereas OSRM provided smoother boundaries of land-cover patches and kept the small land-cover

patches that lost in OHC result. This is particularly well demonstrated by the results in the subarea of Fig. 10(i)-(iii). Comparing the reference map in Fig. 10(i) with Fig. 10(ii)-(iii), it can be seen that the linear building patches in (iii) by OSRM are smoother than those in (ii) and more similar with those in (i). Moreover, the small building patch at the bottom of Fig. 10(ii) by OHC is lost, OSRM, on the contrary, preserved it in Fig. 10(iii).

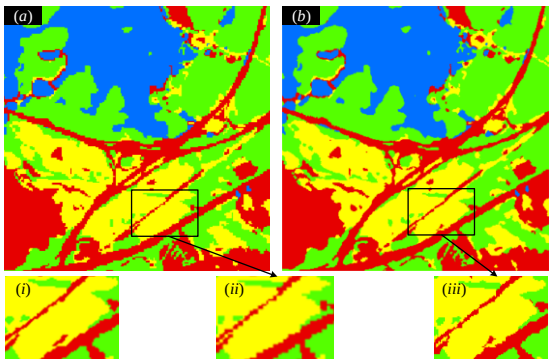

Fig. 10. Classification results for synthetic ZY-3 imagery (S=2). (a) OHC result. (b) OSRM map. (i) The reference map in the subarea marked by the black rectangle in (a) and (b). (ii)-(iii) Classified results in the subarea of (a) and (b), respectively.

2) Accuracy Assessment

Table II gives the OA of classified results for the synthetic ZY-3 image. It can be observed from Table II that OSRM generated higher accuracies than OHC for each scale factor as well. The average OA increase of OSRM is 5.54% over OHC for the three scale factors. Compared with OHC, the OA improvements of OSRM are 7.8%, 5.11% and 3.7% for the scale factor of 2, 3 and 4, respectively.

TABLE II
ACCURACY (OA) FOR THE SYNTHETIC ZY-3 IMAGERY (%)

	OHC	OSRM
S=2	76.99	84.80
S=3	75.98	81.09
S=4	75.23	78.93

D. Experiment 3—Real GF-1 Imagery

An 8-m real GF-1 image, taken over Beijing, China, on October 12, 2015, was tested. Fig. 11(a) exhibits the multispectral GF-1 image (400 ×400 pixels) and contains five main classes of water, vegetation, road, building and bareground. Training samples of the five classes were manually selected from Fig. 11(a) for object-based hard and soft classifications. Performing the OHC on Fig. 11(a), the reference map was generated in Fig. 11(b). Accuracy assessment was implemented on Fig. 11(b). The OA of the reference map was 94.57%, indicating that the reference map in Fig. 11(b) is a reliable dataset for the accuracy assessment of OSRM. Using the two scale factors of 2 and 4, degraded GF-1 images were first produced. Then, image segmentation and object-based hard and soft classifications were performed on each of degraded GF-1 images. Applying the deconvolution technique to the output of object-based soft classified results, semivariograms of the five classes at subpixel scale were estimated

for the two scale factors. Fig. 12 gives the object-based soft classified results for the scale factor of 2. Fig. 13 presents the semivariograms of the five classes and it suggests that deconvolution inferred the effective semivariograms.

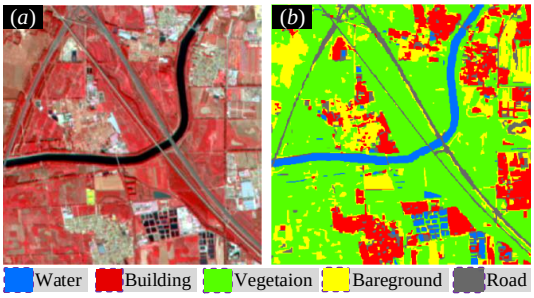

Fig. 11. Experiment on real GF-1 imagery. (a) GF-1 imagery. (b) Reference land-cover map from (a).

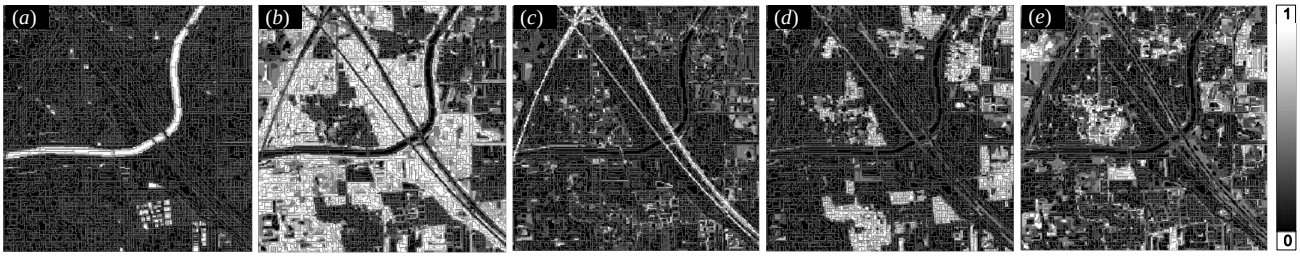

Fig. 12. Object-based soft classification results on real GF-1 imagery (S=2). (a) Water. (b) Vegetation. (c) Road. (d) Building. (e) Bareground.

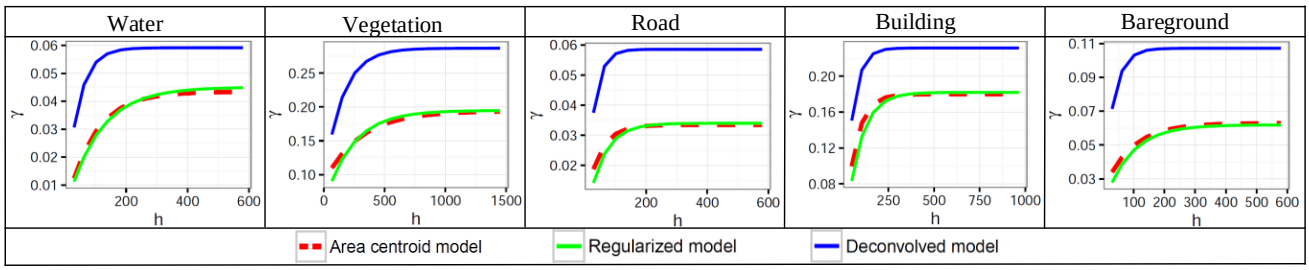

Fig. 13. Deconvolution results for real GF-1 imagery (S=2). The red dash, green solid and blue solid curves are the semivariograms from Fig. 12, regularized semivariograms, and the target point support (subpixel scale) semivariograms from deconvolution, respectively.

1) OSRM Results

Fig. 14 (a) and (b) shows the OHC and OSRM results for the scale factor of 2. It can be found that OSRM once again produced better map than OHC. The OSRM map is finer than the OHC result and OSRM provides more land-cover patches than OHC according to visual assessment. Especially, it can be observed from the lower left of this study area that many small bareground patches are lost in Fig. 14 (a) but preserved in Fig. 14 (b). Moreover, the OSRM map matches better with the reference map in Fig. 11(b) than the OHC results. Compared with the reference map, however, a few noise-induced isolated pixels (e.g., the big bareground patch at the upper left of this study area) were produced by OSRM. The major reasons are that object-based soft classification errors were generated and propagated into the OSRM results and that OSRM used the strict class proportion constraints in determining the optimal class labels of subpixels. Even though, visual assessments indicate that OSRM outperformed the OHC.

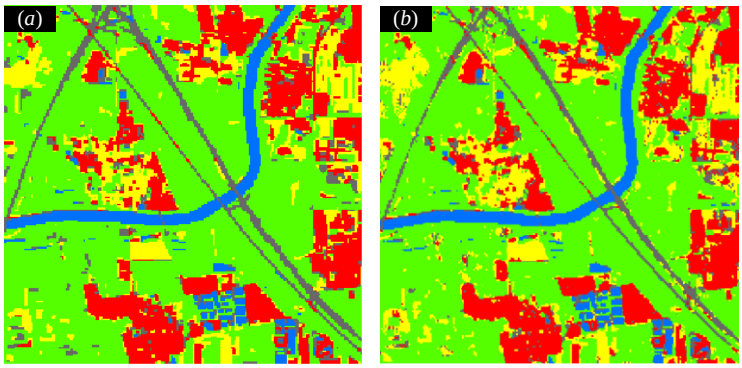

Fig. 14. Classification results for real GF-1 imagery (*S*=2). (a) OHC result. (b) OSRM map.

2) Accuracy Assessment

Table III presents the OA of classified maps for the real GF-1 imagery. Again, OSRM had the highest OA for each scale factor and it generated the average OA increase by 2.77% over OHC. The OA increases of OSRM are 4.24% and 1.31% for scale factors of 2 and 4, respectively.

TABLE III
ACCURACY (OA) FOR REAL GF-1 IMAGERY (%)

	OHC	OSRM
S=2	84.46	88.70
S=4	77.04	78.35

IV. DISCUSSION

A. Sensitivity Analysis of the Segmentation Scale Parameter

Image segmentation is a critical step in object-based classification. The segmentation scale parameter mainly controls the quality of the segmentation results of remote sensing images. Thus, it is necessary to analyze the optimal selection of segmentation scale parameter. In the two experiments on synthetic images, we used the same segmentation scale parameter of 5 for all scale factors. The reason was that it was convenient to analyze the impact of different scale factors on the performance of OSRM through setting the same segmentation scale parameter. In the last experiment on real GF-1 image, the optimal segmentation scale parameters were selected for each image and then the object-based soft classification results were directly derived from the spectral images with the optimal segmentation parameters for each scale factor. The optimal segmentation scale parameter was determined by the *G* function created by combining Moran's I value and variance of object features. More details about the *G* function can be found in [51]. Ten segmentation scale parameters (from 5 to 50 with an interval of 5) were applied to each GF-1 image. Fig. 15 presents the *G* function values in y-axis with the ten segmentation parameters in x-axis for original and degraded GF-1 images. It can be observed from Fig. 15 that the best segmentation scale parameter of the original GF-1 image was 10 because the *G* function achieved the greatest value. For the degraded GF-1 images, the best segmentation scale parameters are 5 and 10 for the scale factor of 2 and 4, respectively.

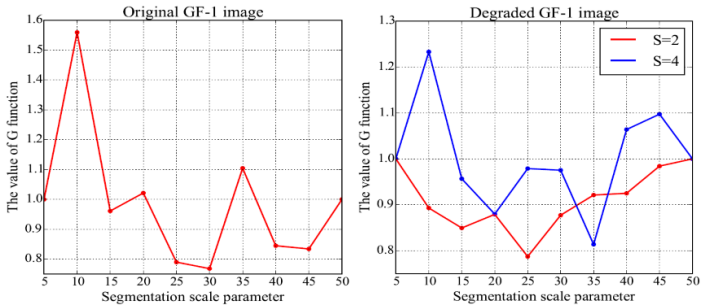

Fig. 15. The optimal segmentation scale parameters for real GF-1 images.

B. *Impact of Scale Factors on OSRM*

Most existing SRM approaches with the pixel-based soft classification results as their inputs are sensitive to scale factors [10, 11, 35]; therefore, the influence of different scale factors on OSRM is analyzed here. Table I, Table II and Table III show that the OA of OSRM gradually decreases with the increase of scale factors. This phenomenon is similar to many pixel-based SRM methods. The major reason may be due to the fact that the complexity and uncertainty of OSRM increase with the increase of scale factors. Focusing on the OA of OSRM in the two experiments on synthetic images, it can be found that the OA of OSRM decreased by 3.1% and 5.87% from S=2 to S=4 for the synthetic ASTER image and ZY-3 image, respectively. With respect to the real GF-1 image, the OA of OSRM reduced by 10.35% from S=2 to S=4. The decrease in the experiment on real GF-1 image is significantly greater than that in the experiments on synthetic images. This is largely caused by the factors of object-based soft classification errors and image segmentation scale parameters. In the first two experiments, the object-based soft classification results were aggregated from the reference maps and error free. On the contrary, the object-based soft classification errors were inevitably generated by directly classifying the spectral GF-1 images. As a result, OSRM maps yield a few the error-induced isolated pixels in the last experiment, as described in Section III.D. The same segmentation scale parameter of 5 was used in synthetic ASTER images and ZY-3 images for all scale factors, while the segmentation scale parameters of 5 and 10 were selected for the scale factor of 2 and 4, respectively. Basically, larger segmentation scale parameter leads to larger objects, which may results in more mixed objects. More mixed objects may add more uncertainty in OSRM process and decrease its accuracy. Although OSRM is sensitive to both scale factors and the segmentation scale parameter, its performance is highly improved comparing with OHC.

V. Conclusion

This paper presents a novel strategy (i.e., OSRM) to implement SRM on objects. OSRM aimed to extend the existing SRM for mixed pixels to predict the class spatial distribution within mixed objects that contain different land-cover classes in object-based classification. OSRM first uses the deconvolution technique to estimate the semivariograms at target subpixel scale for each class according to the class proportions of objects by object-based soft classification. Next, ATPK is employed to predict the soft class values of subpixels within objects in terms of the estimated semivariograms and the class proportions of objects. Finally, a linear

optimization model at object-level is built to obtain the optimal hard class labels of subpixels within each object. Both visual and quantitative assessment of three experimental results indicates that OSRM produced more land-cover details within mixed objects and achieved greater accuracy of classified maps than the traditional object-based hard classification. Therefore, OSRM is an effective solution to estimating the class spatial distribution within mixed objects for the object-based classification of remote sensing images.

ACKNOWLEDGMENTS

REFERENCES

[1] T. Blaschke, "Object based image analysis for remote sensing," *ISPRS Journal of Photogrammetry and Remote Sensing*, vol. 65, pp. 2-16, 2010.
[2] D. Lu and Q. Weng, "A survey of image classification methods and techniques for improving classification performance," *International Journal of Remote Sensing*, vol. 28, pp. 823-870, 2007.
[3] P. Fisher, "The pixel: a snare and a delusion," *International Journal of Remote Sensing*, vol. 18, pp. 679-685, 1997.
[4] P. M. Atkinson, "Mapping sub-pixel boundaries from remotely sensed images," in *Innovations in GIS 4*, London, 1997, pp. 166-180.
[5] T. Blaschke, G. J. Hay, M. Kelly, S. Lang, P. Hofmann, E. Addink, *et al.*, "Geographic object-based image analysis - towards a new paradigm," *ISPRS Journal of Photogrammetry and Remote Sensing*, vol. 87, pp. 180-191, Jan 2014.
[6] A. Tatem, J., H. Lewis, G., P. Atkinson, M., and M. Nixon, S., "Super-resolution target identification from remotely sensed images using a Hopfield neural network," *IEEE Transactions on Geoscience and Remote Sensing*, vol. 39, pp. 781-796, 2001.
[7] P. M. Atkinson, "Sub-pixel target mapping from soft-classified, remotely sensed imagery," *Photogrammetric Engineering and Remote Sensing*, vol. 71, pp. 839-846, 2005.
[8] Y. Ge, Y. Chen, A. Stein, S. Li, and J. Hu, "Enhanced sub-pixel mapping with spatial distribution patterns of geographical objects," *IEEE Transactions on Geoscience and Remote Sensing*, vol. 54, pp. 2356-2370, 2016.
[9] Y. Chen, Y. Ge, G. B. M. Heuvelink, J. Hu, and Y. Jiang, "Hybrid constraints of pure and mixed pixels for soft-then-hard super-resolution mapping with multiple shifted images," *IEEE Journal of Selected Topics in Applied Earth Observations and Remote Sensing*, vol. 8, pp. 2040-2052, 2015.
[10] F. Ling, Y. Du, X. Li, Y. Zhang, F. Xiao, S. Fang, *et al.*, "Superresolution land cover mapping with multiscale information by fusing local smoothness prior and downscaled coarse fractions," *IEEE Transactions on Geoscience and Remote Sensing*, vol. 52, pp. 5677-5692, 2014.
[11] Q. Wang, W. Shi, and L. Wang, "Allocating classes for soft-then-hard subpixel mapping algorithms in units of class," *IEEE Transactions on Geoscience and Remote Sensing*, vol. 52, pp. 2940-2959, 2014.
[12] Y. Zhong, Y. Wu, X. Xu, and L. Zhang, "An adaptive subpixel mapping method based on MAP model and class determination strategy for hyperspectral remote sensing imagery," *IEEE Transactions on Geoscience and Remote Sensing*, vol. 53, pp. 1411-1426, 2015.
[13] F. Ling, X. Li, Y. Du, and F. Xiao, "Sub-pixel mapping of remotely sensed imagery with hybrid intra- and inter-pixel dependence," *International Journal of Remote Sensing*, vol. 34, pp. 341-357, 2013.
[14] A. Tatem, H. Lewis, P. Atkinson, and M. Nixon, "Increasing the spatial resolution of agricultural land cover maps using a Hopfield neural network," *International Journal of Geographical Information Science*, vol. 17, pp. 647-672, 2003.
[15] X. Li, Y. Du, F. Ling, Q. Feng, and B. Fu, "Superresolution mapping of remotely sensed image based on hopfield neural network with anisotropic spatial dependence model," *IEEE Geoscience and Remote Sensing Letters*, vol. 11, pp. 1265 - 1269, 2014.
[16] X. Li, F. Ling, Y. Du, Q. Feng, and Y. Zhang, "A spatial–temporal Hopfield neural network approach for super-resolution land cover mapping with multi-temporal different resolution remotely sensed images," *ISPRS Journal of Photogrammetry and Remote Sensing*, vol. 93, pp. 76-87, 2014.
[17] K. C. Mertens, B. De Baets, L. P. C. Verbeke, and R. R. de Wulf, "A sub-pixel mapping algorithm based on sub-pixel/pixel spatial attraction models," *International Journal of Remote Sensing*, vol. 27, pp. 3293-3310, 2006.
[18] Q. Wang, L. Wang, and D. Liu, "Integration of spatial attractions between and within pixels for sub-pixel mapping," *Journal of Systems Engineering and Electronics*, vol. 23, pp. 293-303, 2012.
[19] Y. Chen, Y. Ge, Q. Wang, and Y. Jiang, "A subpixel mapping algorithm combining pixel-level and subpixel-level spatial dependences with binary integer programming," *Remote Sensing Letters*, vol. 5, pp. 902-911, 2014.
[20] T. Kasetkasem, M. K. Arora, and P. K. Varshney, "Super-resolution land cover mapping using a Markov random field based approach," *Remote Sensing of Environment*, vol. 96, pp. 302-314, 2005.

[21]X. Li, Y. Du, and F. Ling, "Spatially adaptive smoothing parameter selection for Markov random field based sub-pixel mapping of remotely sensed images," *International Journal of Remote Sensing*, vol. 33, pp. 7886-7901, 2012.
[22]V. A. Tolpekin and A. Stein, "Quantification of the effects of land-cover-class spectral separability on the accuracy of Markov-random-field-based superresolution mapping," *IEEE Transactions on Geoscience and Remote Sensing*, vol. 47, pp. 3283-3297, 2009.
[23]L. G. Wang and Q. M. Wang, "Subpixel mapping using Markov random field with multiple spectral constraints from subpixel shifted remote sensing images," *IEEE Geoscience and Remote Sensing Letters*, vol. 10, pp. 598-602, 2013.
[24]Y. Ge, S. Li, and V. C. Lakhan, "Development and testing of a subpixel mapping algorithm," *IEEE Transactions on Geoscience and Remote Sensing*, vol. 47, pp. 2155-2164, 2009.
[25]Y. Ge, Y. Chen, S. Li, and Y. Jiang, "Vectorial boundary-based sub-pixel mapping method for remote-sensing imagery," *International Journal of Remote Sensing*, vol. 35, pp. 1756-1768, 2014.
[26]A. Boucher and P. C. Kyriakidis, "Super-resolution land cover mapping with indicator geostatistics," *Remote Sensing of Environment*, vol. 104, pp. 264-282, 2006.
[27]Y. Ge, "Sub-pixel land-cover mapping with improved fraction images upon multiple-point simulation," *International Journal of Applied Earth Observation and Geoinformation*, vol. 22, pp. 115-126, 2013.
[28]Q. Wang, P. M. Atkinson, and W. Shi, "Indicator cokriging-based subpixel mapping without prior spatial structure information," *IEEE Transactions on Geoscience and Remote Sensing*, vol. 53, pp. 309-323, 2015.
[29]Y. F. Zhong and L. P. Zhang, "Remote sensing image subpixel mapping based on adaptive differential evolution," *IEEE Transactions on Systems, Man, and Cybernetics-Part B: Cybernetics*, vol. 42, pp. 1306-1329 2012.
[30]Y. F. Zhong and L. P. Zhang, "Sub-pixel mapping based on artificial immune systems for remote sensing imagery," *Pattern Recognition*, vol. 46, pp. 2902-2926, 2013.
[31]X. Xu, Y. Zhong, and L. Zhang, "Adaptive subpixel mapping based on a multiagent system for remote-sensing imagery," *IEEE Transactions on Geoscience and Remote Sensing*, vol. 52, pp. 787- 804, 2014.
[32]Q. Wang, L. Wang, and D. Liu, "Particle swarm optimization-based sub-pixel mapping for remote-sensing imagery," *International Journal of Remote Sensing*, vol. 33, pp. 6480-6496, 2012.
[33]Y. Zhang, Y. Du, F. Ling, S. Fang, and X. Li, "Example-based super-resolution land cover mapping using support vector regression," *IEEE Journal of Selected Topics in Applied Earth Observations and Remote Sensing*, vol. 7, pp. 1271-1283, 2014.
[34]Q. Wang, W. Shi, and P. M. Atkinson, "Sub-pixel mapping of remote sensing images based on radial basis function interpolation," *ISPRS Journal of Photogrammetry and Remote Sensing*, vol. 92, pp. 1-15, 2014.
[35]Y. Chen, Y. Ge, and D. Song, "Super-resolution land-cover mapping based on high-accuracy surface modeling," *IEEE Geoscience and Remote Sensing Letters*, vol. 12, pp. 2516-2520, 2015.
[36]F. Ling, Y. Du, X. Li, W. Li, F. Xiao, and Y. Zhang, "Interpolation-based super-resolution land cover mapping," *Remote Sensing Letters*, vol. 4, pp. 629-638, 2013.
[37]J. P. Ardila, V. A. Tolpekin, W. Bijker, and A. Stein, "Markov-random-field-based super-resolution mapping for identification of urban trees in VHR images," *ISPRS Journal of Photogrammetry and Remote Sensing*, vol. 66, pp. 762-775, 2011.
[38]F. Ling, X. Li, F. Xiao, S. Fang, and Y. Du, "Object-based sub-pixel mapping of buildings incorporating the prior shape information from remotely sensed imagery," *International Journal of Applied Earth Observation and Geoinformation*, vol. 18, pp. 283-292, 2012.
[39]C. Huang, Y. Chen, and J. Wu, "DEM-based modification of pixel-swapping algorithm for enhancing floodplain inundation mapping," *International Journal of Remote Sensing*, vol. 35, pp. 365-381, 2014.
[40]L. Y. Li, Y. Chen, T. B. Xu, R. Liu, K. F. Shi, and C. Huang, "Super-resolution mapping of wetland inundation from remote sensing imagery based on integration of back-propagation neural network and genetic algorithm," *Remote Sensing of Environment*, vol. 164, pp. 142-154, Jul 2015.
[41]Y. Ge, Y. Jiang, Y. Chen, A. Stein, D. Jiang, and Y. Jia, "Designing an experiment to investigate subpixel mapping as an alternative method to obtain land use/land cover maps," *Remote Sensing*, vol. 8, p. 360, 2016.
[42]C. E. Woodcock and A. H. Strahler, "The factor of scale in remote sensing," *Remote Sensing of Environment*, vol. 21, pp. 311-332, Apr 1987.
[43]N. Clinton, A. Holt, J. Scarborough, L. Yan, and P. Gong, "Accuracy assessment measures for object-based image segmentation goodness," *Photogrammetric Engineering and Remote Sensing*, vol. 76, pp. 289-299, Mar 2010.
[44]G. M. Espindola, G. Camara, I. A. Reis, L. S. Bins, and A. M. Monteiro, "Parameter selection for region-growing image segmentation algorithms using spatial autocorrelation," *International Journal of Remote Sensing*, vol. 27, pp. 3035-3040, Jul 20 2006.
[45]N. P. Truong, G. B. M. Heuvelink, and E. Pebesma, "Bayesian Area-to-Point Kriging Using Expert Knowledge as Informative Priors," *International Journal of applied Earth Observation and Geoinformation*, vol. 30, pp. 128 - 138, 2014 2014.
[46]P. C. Kyriakidis, "A geostatistical framework for area-to-point spatial interpolation," *Geographical Analysis*, vol. 36, pp. 259-289, 2004.
[47]P. Goovaerts, "Kriging and semivariogram deconvolution in the presence of irregular geographical units," *Mathematical Geosciences*, vol. 40, pp. 101-128, 2008.
[48]A. G. Journel and C. J. Huijbregts, *Mining geostatistics*. London: Academic Press, 1978.

[49]Q. Wang, W. Shi, and L. Wang, "Indicator cokriging-based subpixel land cover mapping with shifted images," *IEEE Journal of Selected Topics in Applied Earth Observations and Remote Sensing*, vol. 7, pp. 327-339, 2014.
[50]P. M. Atkinson and D. K. Naser, "A geostatistically weighted k-NN classifier for remotely sensed imagery," *Geographical Analysis*, vol. 42, pp. 204-225, Apr 2010.
[51]Y. Chen, Y. Ge, and Y. Jia, "Integrating object boundary in super-resolution land cover mapping," *IEEE Journal of Selected Topics in Applied Earth Observations and Remote Sensing*, p. doi: 10.1109/JSTARS.2016.2533571, 2016.